Measuring and Imaging Permittivity of Insulators Using High-Frequency Eddy-Current Devices

Simone Gäbler, Henning Heuer, *Member, IEEE*, and Gert Heinrich

***Abstract*— This paper shows that the high-frequency eddy-current (HFEC) measurement devices can be used not only for characterizing conductivity and magnetic permeability related properties of electrically conductive materials, but also for permittivity characterization of insulators. Maxwell's equations, finite-element method simulations, and experimental research are applied to support this hypothesis. An industrial HFEC device is used to measure the change of dielectric properties during the curing process of the epoxy resin L20. The measurement results are in good agreement with the expected behavior of the parameters relative permittivity and tan δ during cure. Using a capacitive reference device, similar characteristics regarding the change of the complex permittivity of the resin can be observed. In addition, HFEC imaging results on polymethyl methacrylate are presented, discussed, and compared with capacitive imaging. HFEC permittivity mapping benefits from a high spatial resolution with a sensitivity and penetration depth that is at least comparable with those of capacitive imaging technology.**

***Index Terms*— Dielectric constant, dielectric losses, dielectric measurement, EC measurement, eddy currents (ECs), electromagnetic fields, electromagnetic induction, electromagnetic measurement, epoxy curing, epoxy resins, impedance measurement, insulators, nondestructive testing, parasitic capacitance, permittivity, polymers.**

I. Introduction

EDDY current (EC) technology is the standard nondestructive evaluation of electric conductivity and magnetic permeability related properties in conductive materials [1], [2]. However, this restriction to electrically conductive materials is also the most cited weakness of EC measurement in comparison with other electromagnetic technologies, e.g., [3]–[5]. As this paper will demonstrate, this disadvantage can be overcome, when using EC devices, which operate in the high-frequency range (3–30 MHz [6]). In addition to the classical fields of application, the permittivity characterization on insulating and low-conductive materials becomes possible.

The technologies, which are currently prevalent for permittivity measurement on insulating materials, are either lumped or distributed circuit methods. The former use a capacitive setup whereas the latter rely on wave propagation principles in the microwave or terahertz frequency range [7]. Both approaches struggle to penetrate electrically conductive materials. In addition, the lumped circuit methods are limited in spatial resolution. Standard lumped circuit methods operate in the low-frequency range and usually require an excellent electrical contact between the electrodes and the sample [8]. When using an appropriate calibration, high measurement accuracy of 0.1% regarding magnitude and 0.06° regarding phase can be achieved at nonconductive materials [9]. Applied to conductive materials, capacitive methods face the issue of electrode polarization [7], [10]. In addition, two-side access to the sample is required, when using parallel plate electrodes. Interdigital capacitive sensors overcome this obstacle, resulting in a lower penetration depth [11]. For imaging purposes, the preferred methods do not require electrical contact to the sample. For the low- to mid-frequency range, single-sided stray-field capacitive imaging is available. This method is mainly used for mapping permittivity variations in nonconductive materials or sandwich structures. However, the use on conductive materials is mainly limited to surface characterization as charges accumulate there. The penetration depth of capacitive imaging on insulating materials increases in correspondence with the electrode size, but it must be carefully traded off against a decreasing spatial resolution [12]. Another group of permittivity measurement technologies are distributed circuit methods, which operate at the microwave or terahertz frequency band [7]. Microwave measurement approaches use either open or closed structures to characterize the permittivity of the material of interest [13]. Closed structures like the cavity perturbation technology or waveguide and coaxial transmission line methods usually require a particular sample preparation and geometry [14]. Consequently, they are not suitable for measuring complex parts or large area applications. Open structures, such as open-ended probe reflection systems or free-space transmission systems, are generally suitable for imaging and operate in the electromagnetic near or far field. The spatial resolution in the far field depends on the measurement frequency and is generally limited to about half of the wavelength, resulting in ~15 mm at 10 GHz [15], [16]. Consequently, high-resolution

Manuscript received April 1, 2014; revised November 12, 2014; accepted November 17, 2014. Date of publication March 4, 2015; date of current version July 10, 2015. This work was supported in part by the Dresden University of Technology, Dresden, Germany, through the Program for the Promotion of Young Female Scientists and in part by the Suragus GmbH. The Associate Editor coordinating the review process was Dr. Reza Zoughi.

S. Gäbler is with the Leibniz Institute of Polymer Research, Dresden 01069, Germany and also with the Fraunhofer Institute for Ceramic Technology and Systems, Dresden 01277, Germany (e-mail: gaebler@ipfdd.de).

H. Heuer is with the Fraunhofer Institute for Ceramic Technology and Systems, Dresden, Germany, and also with the Dresden University of Technology, Dresden 01069, Germany (e-mail: henning.heuer@ikts-md.fraunhofer.de).

G. Heinrich is with the Leibniz Institute of Polymer Research, Dresden 01069, Germany, and also with the Dresden University of Technology, Dresden 01069, Germany (e-mail: gheinrich@ipfdd.de).

Color versions of one or more of the figures in this paper are available online at http://ieeexplore.ieee.org.

Digital Object Identifier 10.1109/TIM.2015.2390851

far-field imaging requires higher measurement frequencies, which is more expensive [15]. In the near field, the spatial resolution is mainly determined by the geometry of the probe. Thus, microwave near-field imaging achieves a high spatial resolution already at lower microwave frequencies [4], [15]. Typical for near-field microwave imaging is a reflective setup with open-ended rectangular wave guides or open-ended coaxial probes [5], [17], [18]. A spatial resolution of 1 mm or less and a penetration depth of several millimeters are reported for insulating materials [19]. With evanescent microwaves probes, which are generated at the end of a microstrip resonator, even a lateral spatial resolution of 0.4 μm could be reached [4]. However, with smaller probes, the lateral resolution improves at the cost of the penetration depth [18]. In general, the reflective setups are sensitive to variations in the standoff distance between the probe and the sample [15]. Using a dual-polarized microwave reflectometer, this influence can be eliminated [5]. Although microwaves are generally not able to penetrate through conductive materials [11], [15] or materials with a very high dielectric loss [18], some of the near-field methods allow characterization of unidirectional carbon-fiber-reinforced polymers (CFRPs). In this case, the electrical field polarization needs to be perpendicular to the carbon fibers [5], [15]. Hence, it works for unidirectional stacks, but fails at laminates with changing fiber directions, where penetration is not possible [15]. In addition to reflective setups, transmission technologies can be used for imaging purposes as well [20], [21]. Due to diffraction effects at the edges of the samples, they are most suitable for large flat specimens [14]. The last group of dielectric imaging technologies, which shall be mentioned here, is terahertz imaging. It allows a higher spatial resolution than microwave testing in the far field due to the higher measurement frequency, but the hardware is still significantly more expensive. Similar to microwave imaging, it is generally restricted to electrically nonconductive materials or surface characterization of electrically conductive materials. An exception is the terahertz time-domain spectroscopy that penetrates several layers of CFRP [22].

Comparing high-frequency EC (HFEC) measurement to the prevalent and previously discussed methods to characterize permittivity, two potential advantages become obvious: EC allows a high spatial resolution [23], when compared with the lumped circuit methods and a good penetration depth in conductive materials. The reason can be found in the lower frequency and therefore, higher standard penetration depth of EC compared with microwave or terahertz technologies [24], [25]. However, the real penetration depth of EC further depends on the diameter of the sensor, as an EC sensor does not generate a plane electromagnetic wave [25], [26]. The penetration depth increases with the sensor size, at best reaching the standard penetration depth. Nevertheless, previous researchers reported a significant penetration depth in CFRP while maintaining a high spatial resolution [24], [27]. Structural defects or inclusions in multidirectional CFRP up to 8 mm below the surface were detected [28]. As most of the briefly introduced technologies for permittivity characterization, the EC measurement is contact free, allows a single-sided inspection [27], and does not require any special sample preparation [29]. However, usually it is solely used on conductive samples and the influence of the sample permittivity is neglected [1], [2]. A potentially significant influence of sample permittivity on EC measurement was only reported in the context of characterizing CFRP [23], [24], [30], [31]. The reason for this effect is seen in the conductive and capacitive network formed by the carbon rovings (bundles of carbon fibers) [30].

The aim of this paper is to prove that permittivity related effects of low and nonconductive samples should not be neglected when using an HFEC device. They are rather strong enough to serve for permittivity characterization on insulating materials as we will show in the following sections. Starting with a description of electromagnetic fundamentals, the theoretical approach is followed by a discussion of results from finite-element method (FEM) simulations. Then, this paper will focus on the experimental monitoring of a curing epoxy resin to demonstrate the feasibility of the presented approach. Finally, the possibility of permittivity imaging is presented, and the results are discussed in comparison with capacitive imaging technology.

II. Theoretical Influence of Sample Permittivity on Coil Impedance

Maxwell's equations for constant frequencies demonstrate that sample conductivity and permittivity influence the EC measurement.

Maxwell's equations describe the fundamentals of electromagnetic theory [32]

$$\nabla \cdot \boldsymbol{D} = \rho \tag{1}$$

$$\nabla \cdot \boldsymbol{B} = 0 \tag{2}$$

$$\nabla \times \boldsymbol{E} = -j\omega \boldsymbol{B} \tag{3}$$

$$\nabla \times \boldsymbol{H} = \boldsymbol{J} + j\omega \boldsymbol{D}. \tag{4}$$

The above equations are combined with the following constitutive equations:

$$\boldsymbol{B} = \underline{\mu} \boldsymbol{H} \tag{5}$$

$$\boldsymbol{D} = \underline{\varepsilon} \boldsymbol{E} \tag{6}$$

$$\boldsymbol{J} = \sigma \boldsymbol{E}. \tag{7}$$

Attention shall be drawn into two facts.

1) A magnetic field $\boldsymbol{H}$ with the magnetic flux density $\boldsymbol{B}$, varying in time with the angular frequency ω (as it is caused by the ac in the coil) creates a rotating electric field $\boldsymbol{E}$ independent of the conductivity of the sample (3). This electric field is the source for ECs with the current density $\boldsymbol{J}$, as well as for electric displacement fields $\boldsymbol{D}$ and, respectively, displacement currents with the density $\boldsymbol{J_D} = j\omega \boldsymbol{D}$. The current density $\boldsymbol{J}$ depends on the conductivity of the sample σ (7), whereas the displacement current density $\boldsymbol{J_D}$ depends on the permittivity $\underline{\varepsilon}$ of the material to be tested (6).
2) Both the ECs and the displacement currents are associated with a magnetic field $\boldsymbol{H}$ also influencing the coil's magnetic field (4); and therefore, the coil impedance.

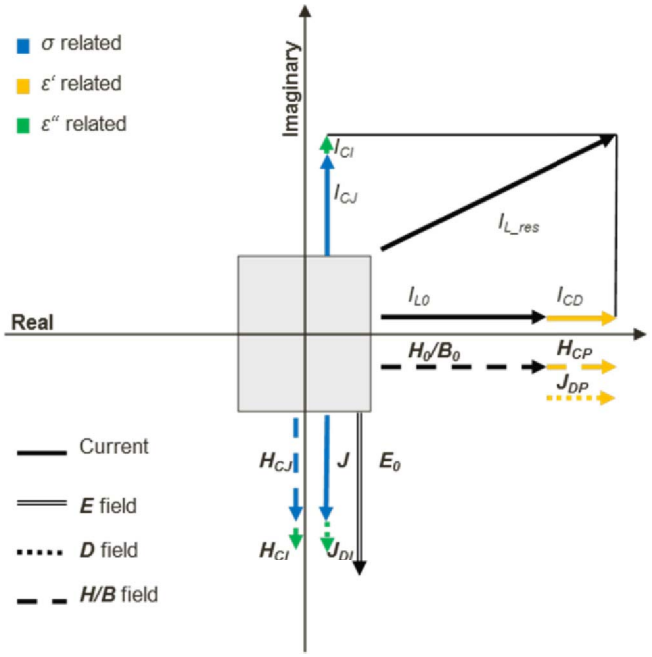

Fig. 1. Impedance plot: phase characteristics of electromagnetic effects occurring during HFEC measurement.

Although both conductivity and permittivity of the sample influence the coil impedance, they affect the EC measurement signal in different ways. The reasons are differences in the frequency dependence and within the phase shift of the two factors.

Both the magnitudes of EC density $\boldsymbol{J}$ and displacement current density $\boldsymbol{J_J}$ are frequency dependent. They behave proportional to the intensity of the electric field $\boldsymbol{E}$, which depends on the rate of change of the magnetic flux density $\boldsymbol{B}$ (3). Whereas EC density $\boldsymbol{J}$ is directly related to the electric field intensity $\boldsymbol{E}$ (7), the displacement current density $\boldsymbol{J_J}$ depends on the rate of change of the electric field

$$\nabla \times \boldsymbol{H} = \boldsymbol{J} + \boldsymbol{J_D} = \sigma \boldsymbol{E} + j\underline{\varepsilon}\omega \boldsymbol{E}. \tag{8}$$

Thus, the excitation frequency has much more impact on the ability to measure permittivity using EC technology, than to measure conductivity related effects of the sample. Subsequently, this might explain why displacement currents can be neglected at the lower frequency ranges, which are typically used for EC inspection of metallic materials. However, when using higher frequencies permittivity related effects of the sample become relevant, especially in low-conductive materials.

Even more relevant is the phase shift of the magnetic field in response to ECs compared with the one caused by displacement currents. Ideally, without dielectric losses, the magnetic field change resulting from the displacement currents is delayed by 90° compared with that caused by ECs. As a consequence, an increase in permittivity empowers the initial magnetic field, whereas a rise in conductivity weakens the magnetic field created by the coil.

To better understand this effect, it is useful to follow the phase characteristics of each physical phenomenon step by step during EC measurement (Fig. 1). First, the current flowing initially through the probing coil I_{L0} is defined on the real axis, thus having a phase of 0°. The magnetic field with the strength $\boldsymbol{H_0}$, as well as the magnetic flux density $\boldsymbol{B_0}$ (5), arising from the coil, are in phase with their source, the current.[1] Another behavior shows the electric field with the strength $\boldsymbol{E_0}$. It is shifted by −90° compared with its feeding alternating magnetic field (3). Exposed to a sample, the electric field leads to ECs with the density $\boldsymbol{J}$ and displacement currents with the density $\boldsymbol{J_D}$. As the permittivity of the sample is a complex value (9), the displacement current density $\boldsymbol{J_D}$ is complex as well. The component $\boldsymbol{J_{DP}}$ is proportional to the real part of complex permittivity ε'. The component $\boldsymbol{J_{Dl}}$ represents the dielectric losses and depends on the imaginary part of complex permittivity ε''

$$\underline{\varepsilon} = \varepsilon' - j\varepsilon'' \tag{9}$$

$$\boldsymbol{J_D} = j\underline{\varepsilon}\omega \boldsymbol{E} = j\varepsilon'\omega \boldsymbol{E} + \varepsilon''\omega \boldsymbol{E} = \boldsymbol{J_{DP}} + \boldsymbol{J_{Dl}}. \tag{10}$$

Dielectric losses $\boldsymbol{J_{Dl}}$ and EC density $\boldsymbol{J}$ occur in phase with the electric field. Together they represent the current density resulting from the effective conductivity $\sigma + \varepsilon''\omega$. In contrast, the displacement current $\boldsymbol{D_{DP}}$ that is proportional to the real part of permittivity is characterized by a phase shift of 90° compared with the electric field.

Each of those effects causes a change in the magnetic field strength $\boldsymbol{H_C}$, which is in phase with its source (8). Thus, compared with the initial magnetic field, the changes resulting from the real part of samples permittivity $\boldsymbol{H_{CP}}$ empower the initial field as they have the same phase and direction. The magnetic fields resulting from the conductivity $\boldsymbol{H_{CJ}}$ and the dielectric loss $\boldsymbol{H_{Cl}}$ of the sample are shifted in phase by −90° compared with the coil's field without sample exposure. Consequently, they weaken the magnetic field of the coil and cause a phase shift of the resulting current I_{L_res}, which is comparable with that resulting from higher ohmic losses within the coil [29], [33].

III. FEM Simulation

To test our conclusions drawn in Section II and to better understand the influence of complex factors like parasitic and interwinding capacitances within the coil, FEM modeling was used. It was found that probes with a maximum of two layers (in the radial direction) ensure that the permittivity measurement with EC technology is not dominated by interwinding capacitances within the coil. In addition, the FEM results confirm that an increase of the permittivity of a sample (real part) empowers the magnetic field in the coil.

A. Model and Solver Description

For FEM simulation, the EC module from ANSYS Maxwell 3-D 16.0 was used. Compared with the low-frequency modules from ANSYS Emag, Opera, and Flux 3-D this is the only module, where Maxwell's equations are fully implemented. Thus, the displacement currents are being considered [34]. Compared with many high-frequency modules, the EC module of ANSYS Maxwell has the

[1] Disregarding the imaginary part of complex permeability μ.

advantage of simplified (stranded) modeling and analysis of probing coils, reducing the calculation time significantly.

The model consist of a stranded coil (a hollow copper cylinder with an outer radius of 3.9 mm, an inner radius of 2.35 mm, and 3.2-mm height, excited by an sinusoidal current of 100 mA per winding and 2.8 A in total), a cup core of ferrite material ($\mu_r = 95$, outer radius of 4.7 mm, 0.7-mm wall thickness, and 4.7-mm height) and a sample of 60 mm × 60 mm × 3 mm, positioned with a 0.4-mm liftoff to the probing coil. In addition, a 100% region was used, limiting the virtual space, where Maxwell's equations are solved. The Neumann boundaries were assigned to the outside of this region. Adaptive meshing was applied, using a maximum number of 25 passes to reach the defined error limit of 0.1%. Depending on the scope, the described model was adapted or expanded slightly, as explained in the following sections.

B. Relevance of Electric Fields Resulting From Interwinding Capacitances Within the Eddy Current Probe

A coil within an ac circuit does emit not only a primary electric field, which is linked to the primary magnetic field, but also a parasitic electric field due to its interwinding capacitances. The simulation reveals that this parasitic electric field can be even stronger than the primary electric field, depending on the design of the coil. This capacitive effect influences the permittivity measurement, especially at high frequencies. To narrow the gap between the simulation and the experiments, the probe coils used have to fulfill certain design criteria to ensure that the permittivity measurement is dominated by inductive effects and not by interwinding capacitances.

To evaluate whether the interwinding capacitance of an EC probe (ECP) has a significant effect on the objective to measure sample permittivity using HFEC, the parasitic as well as the primary electric fields were simulated and compared. The primary field was modeled using the EC solver as described above. As there is no possibility to simulate interwinding capacitances within the probe using this solver, the model was extended using an electrostatic solver. There, the parasitic electric field was modeled assuming the worst case of two adjacent wires having the opposite potential (+5 and −5 V). Compared are the magnitudes of the electric fields in both scenarios 0.4 mm away from the coil/the wire and the direction of the field vectors.

The simulation shows that the parasitic electric vector field of the ECP has another direction within the object under test than the primary electric field, but it has higher field strength (Fig. 2). Based on the model of two adjacent wires with an opposite potential, the maximum magnitude of the parasitic electric field strength is almost 20 times higher than the maximum magnitude of the primary electric field, which is part of the electromagnetic wave created by the coil. Whereas the primary electric field is an eddy field sweeping around the magnetic vector field, the parasitic electric field is orthogonal to the sample.

Modeling the interaction of the primary and the parasitic electric field is not possible in ANSYS, as the electrostatic module cannot be combined with the EC module. This makes it difficult to conclude whether the interwinding capacitance improves or disturbs the permittivity measurement with an ECP. The aim of this paper is to demonstrate that the permittivity measurements are possible using the inductive mechanisms ($\boldsymbol{E} \times \boldsymbol{H}$ field) of an ECP, thus the parasitic electric field needs to be reduced to a minimum.

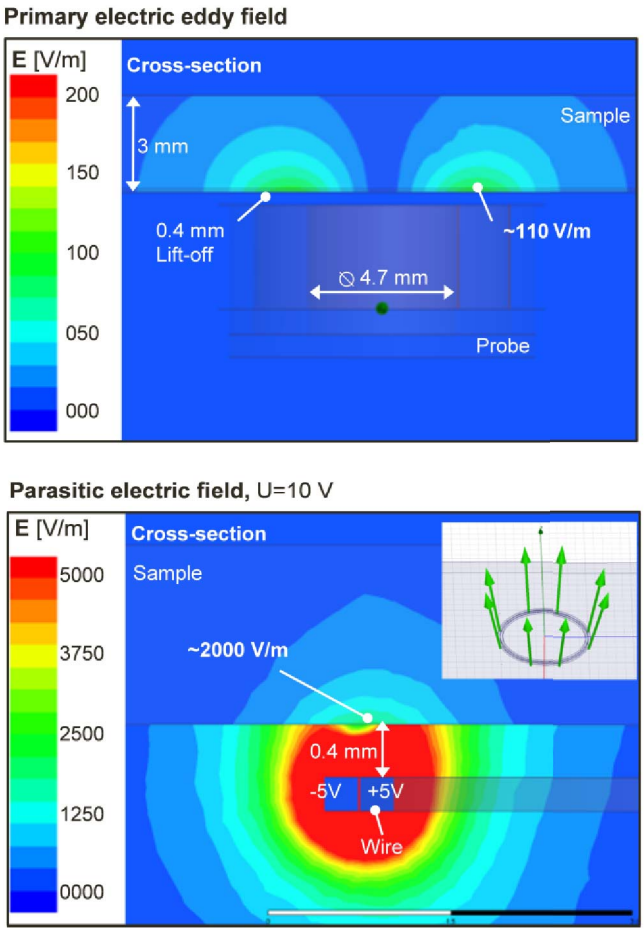

Fig. 2. Magnitude of the primary electric eddy field within the object under test (top) compared with the magnitude (bottom) and direction (bottom, inset) of the parasitic electric field resulting from the interwinding capacitance of the coil.

To reduce the parasitic electric field, the wire length l between the two adjacent windings has to be optimized. At a given wavelength, this is the factor determining the potential difference. Consequently, it determines the parasitic electric field between the adjacent windings, as the voltage with the peak value $\hat{u}$ is propagating sinusoidal through the wire

$$U = \hat{u}\left(\sin\left(\omega t_0 + \frac{2\pi l}{\lambda}\right) - \sin(\omega t_0)\right). \tag{11}$$

The modeled maximum of $U = 10$ V [+5 and −5 V] between adjacent wires in a probe only appears when the distance between the adjacent wires l is half of a wavelength λ. For a measurement frequency of 10 MHz, the corresponding wire length between the two adjacent windings is ∼15 m. This would be the case for a coil with 60 windings per layer and 4 cm in diameter, which is not appropriate for

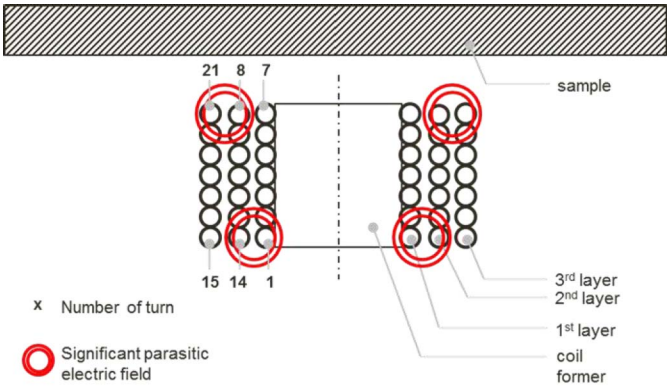

Fig. 3. Vertical cross section of a coil explaining the influence of the number of layers on the interwinding capacitances next to the coil.

high-frequency measurements. Nevertheless, here, the voltage would reach its maximum in one wire, whereas it would be passing the minimum in the other one. Thus, to minimize the potential difference U, the wire length between the two adjacent windings should be as small as possible. This can be achieved by fulfilling the following two design criteria.

1) Avoiding more than two layers of windings.
2) Keeping the coil diameter small.

The condition of using ECPs with a maximum of two layers to minimize interwinding capacitances is related to the way the probing coils are built up. They are wound by first applying a full layer of windings on the coil former, e.g., from bottom to top, and then applying the second layer from top to bottom, and so on. Thus, a coil consisting of two layers typically has the adjacent turns with the maximum difference in potential not situated next to the sample, but on the opposite side of the coil. When adding a third layer to the coil, for the first time, the two adjacent windings next to the sample have a significant wire length l in between. This results in a significant voltage difference (Fig. 3).

Reducing the coil diameter without removing the third layer reduces the parasitic electric field significantly but not sufficiently. Assuming a coil diameter of ~6 mm and 10 turns per layer, the wire length l between the two adjacent winding is ~0.38 m (π^*d^*20). At 10 MHz, this is about one-hundredth of the wave length, leading to a maximum voltage difference between the adjacent wires <0.4 V. This is more than 20 times less compared with the +5/−5 V scenario but still sufficient to create an electric field with almost the same strength as the primary electric field of the ECP.

C. Change of the Magnetic Flux Passing Through the HFEC Probe Due to Permittivity Variations

The simulation results support the conclusions drawn in Section II. With increasing sample permittivity (real part) an increasing magnetic flux is passing through the HFEC probe. Increasing dielectric losses weaken the magnetic flux similarly as an increase of sample conductivity.

The previously described model was used in the simulation. Six homogenous samples were defined, showing differences in complex relative permittivity and bulk conductivity (Table I). Relative magnetic permeability μ_r was kept constant at $\mu_r = 1$.

TABLE I
SAMPLE CHARACTERISTICS AND CALCULATED MAGNETIC FLUX

Sample	ε_r'	tan δ	σ [kS/m]	Re(ϕ) 10^-8 Wb	Im(ϕ) 10^-16 Wb
I	1	0	0	1.8221949	0.00
II	4.2	0	0	1.8221959	0.00
III	1	0.02	0	1.8221949	-0.56
IV	1	0.02	70	0.1742454	-1.79E+07
V	4.2	0.02	0	1.8221959	-2.37
VI	8.4	0.02	0	1.8221971	-4.74

TABLE II
MAGNETIC FLUX DIFFERENCES DEPENDING ON THE SPECIFIC PARAMETER THAT IS CHANGED

	Parameter change			Δ|ϕ|	|Δϕ|
Scenario	$\Delta\varepsilon_r'$	$\Delta\varepsilon_r''$	Δ σ [kS/m]	10^-14 Wb	10^-14 Wb
II-I	**3.2**	0.00	0	0.90	0.90
III-I	0	**0.02**	0	-1.03E-08	5.64E-03
IV-III	0	0.00	**70**	-1.57E+06	1.66E+06

The magnetic flux Φ passing through the horizontal cross section S of the coil was calculated at $f = 10$ MHz using the field calculator

$$\Phi = \iint_S \boldsymbol{B} d\boldsymbol{S}. \tag{12}$$

The calculated magnetic flux passing through the coil decreases with increasing sample conductivity (Table II, scenario IV-III) and is shifted away from the real axis (Table I, sample IV).

The flux differences caused by a change of sample permittivity are quite small with $\sim 10^{-14}$ Wb, which is a challenge for experimental evaluation. It will be important to strictly eliminate drift effects and to use a measurement setup that allows a very good signal-to-noise ratio. To eliminate drift effects like temperature changes regular reference or calibration measurements are needed. To achieve a good signal-to-noise ratio, there are two factors that should be considered.

1) It is important that the processed signal consists mainly of the change of the signal due to sample permittivity. It should not contain the total signal that is generated in the coil, as this is the orders of magnitudes bigger. Therefore, a thoroughly adjusted balancing coil is needed that can compensate for a good portion of the signal in air [35].
2) It is critical to minimize noise by carefully selecting the components for the analog signal processing like cables, amplifiers, and the analog-to-digital converter. However, from a simulation point of view, the calculated flux differences are significant. The calculations of magnetic flux are reproducible up to about 10^{-30} Wb difference, so the results are about the factor 10^{16} away from the range of numerical error.

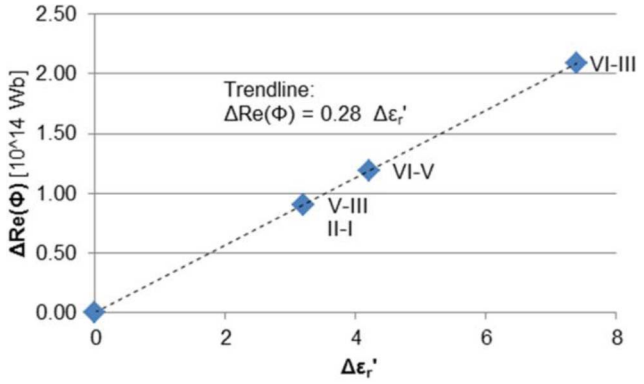

Fig. 4. Change of real part of the magnetic flux passing through the coil showing a linear dependence on the change of the real part of permittivity for nonconductive samples.

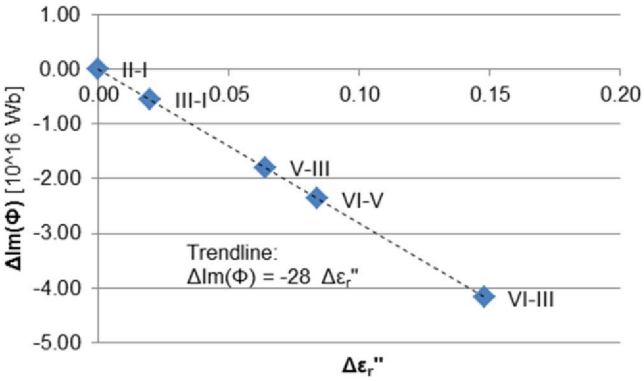

Fig. 5. Change of imaginary part of the magnetic flux passing through the coil showing a negative linear dependence on the change of the imaginary part of permittivity for nonconductive samples.

By analyzing the calculated magnetic flux differences, three conclusions can be drawn for nonconductive samples.

1) The difference in magnitude of the magnetic flux $\Delta|\Phi|$ is negative when the dielectric loss ε_r'' increases celsius paribus (c.p.), but positive when the real part of permittivity ε_r' increases (Table II). Hence, an increasing dielectric loss weakens the magnetic flux Φ passing through the coil where increasing sample permittivity empowers it.
2) The change of the real part of the magnetic flux passing through coil $\Delta\mathrm{Re}(\Phi)$ is mainly influenced by the change of the real part of permittivity $\Delta\varepsilon_r'$ (Fig. 4) and shows a linear dependence on this variable within the analyzed limits. The flux change does not depend on the initial permittivity.
3) The change of the imaginary part of the magnetic flux passing through coil $\Delta\mathrm{Im}(\Phi)$ shows a negative linear correlation with the imaginary part of permittivity $\Delta\varepsilon_r''$ within the analyzed limits (Fig. 5).

IV. Monitoring Permittivity Change of a Curing Epoxy Resin

Based on Maxwell's equations and on the FEM simulation, it was shown that it is theoretically possible to measure permittivity on insulators or composites using HFEC. The following section gives a first experimental proof. By monitoring the curing process of an industrial epoxy amine resin system, we demonstrate that permittivity data obtained with HFEC devices are comparable with those obtained with a standard capacitive sensor.

The cure monitoring was selected, because it is a time-dependent process; i.e., it provides the opportunity to measure a permittivity change within one specific sample, avoiding typical sources for error in HFEC measurement. Such errors might be caused, for example, by differences in sample geometry and unintended differences in the experimental setups like liftoff, sample-to-sensor position, and so on. In addition, the selected task does not require directly measuring quantitatively, as the permittivity change during cure has a characteristic pattern overtime. Thus, a qualitative comparison with the reference method is possible.

A. Expected Permittivity Change of Epoxy Resins During Cure

To explain the change of dielectric properties during cure of an epoxy resin, the following topics are briefly introduced: 1) factors determining the permittivity of a material; 2) the curing process of an epoxy; and 3) the resulting permittivity changes during cure.

Permittivity describes how a material responds to an external electric field. It is a complex quantity resulting from the molecular mechanisms of polarization and charge migration. Charge migration occurs mainly at lower frequencies in the form of ionic conduction. Polarization is caused by dipole orientation, either of permanent dipoles or induced ones [36], [37]. An extensive overview on molecular and environmental factors that are determining the permittivity of a material as well as on existing models can be found in [10]. To understand the expected permittivity change during cure, it is important to know that the permittivity of a material is frequency dependent, which is described by characteristic dielectric relaxation times within a variety of semiempirical equations [7]. Reaching a certain frequency, a growing number of permanent dipoles cannot move fast enough, hence permittivity is decreasing. At the same time, polarization losses increase, so the imaginary part of the permittivity is reaching a local maximum [10]. The dielectric relaxation times increase with increasing molecular weight and increasing viscosity [38].

During the curing reaction of an epoxy resin and a hardener, the concentration of the reactants is decreasing whereas the concentration of the usually less polar end product [39] is increasing. Due to the cross-linking process, molecular weight is rising, resulting among others in an augmentation of viscosity. As the reaction is exothermic, heat is produced [37].

These micro and macromolecular changes occurring within an epoxy during cure affect the permittivity in three different ways: 1) ionic conduction decreases; 2) dielectric relaxation times of the reactive system decline; and 3) the relative permittivity drops as well [37], [39]–[41].

The decrease of ionic conduction is only visible in the low-frequency range, thus this mechanism cannot be used for

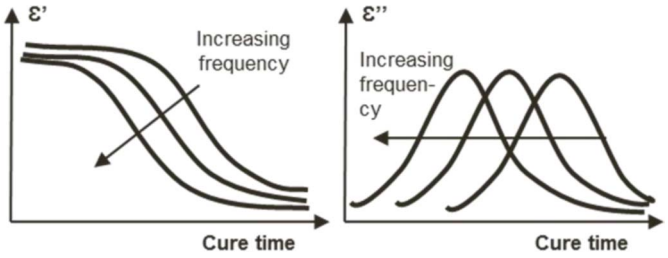

Fig. 6. Progress of complex permittivity during cure [38], [39].

HFEC measurements [39]. However, especially, when using capacitive setups, scientists often rely on the change of ionic conduction to monitor the curing process [41]–[43].

More relevant for HFEC measurement is the phenomenon of declining relaxation times. It can be observed as a peak of the imaginary part of permittivity measured at a constant frequency during cure (Fig. 6). The peak indicates the point in time when the current relaxation time is equal to the reciprocal of the frequency (in rad). Thus, at higher frequencies, the peak occurs earlier than at lower ones (relaxation time has already increased so that the molecular motion cannot follow a higher frequency anymore but still can follow a lower one).

The second effect that can be used to monitor the cure of an epoxy with HFEC devices is the drop of the real part of permittivity. In the early stage of reaction, only a slight decrease of permittivity is observed, which results from the concentration change of reactants and the usually less polar end product. Later during cure, due to the increasing relaxation times and vitrification of the system, the permittivity decreases much more abruptly. Molecular motion cannot keep up with the measurement frequency anymore [39]. As explained for the loss peak, with increasing frequency, this phenomenon can be noticed earlier in the curing process (Fig. 6).

Although dielectric cure monitoring is widely used, influences of the electromagnetic field on the sample cannot generally be neglected and should be evaluated regarding the specific material of interest. In particular, liquid-crystal thermosets show strong orientation effects on a microscopic level, resulting in a change of macroscopic properties, when cured under the influence of alternating electric fields or strong static magnetic fields [44], [45]. In addition, the alignment of certain filler materials like carbon black [46] or carbon nanotubes [47] can be influenced by applying ac electric fields during cure. In addition, the electric fields can generate heat in polymeric samples due to dielectric losses. Hence, they can influence the curing process itself. This principle is used, for example, in microwave heating/curing [48]. However, for frequencies below the microwave range, and for the small electric fields that are used for dielectric cure monitoring, this effect of heat generation can be neglected.

B. Experimental Setup

An industrial epoxy amine resin system (L20 and EPH 161 distributed by R&G, Waldenbuch, Germany) was manually mixed following the prescribed weight ratio of 100:25. It was cured at room temperature afterward. During the curing process, the change of its permittivity was measured using a capacitive measurement setup and an HFEC device. The full set of measurements with the two different devices was not conducted on the same day nor at the same sample. Thus, the results may vary slightly between both approaches, as small deviations in stoichiometric composition or room temperature are possible.

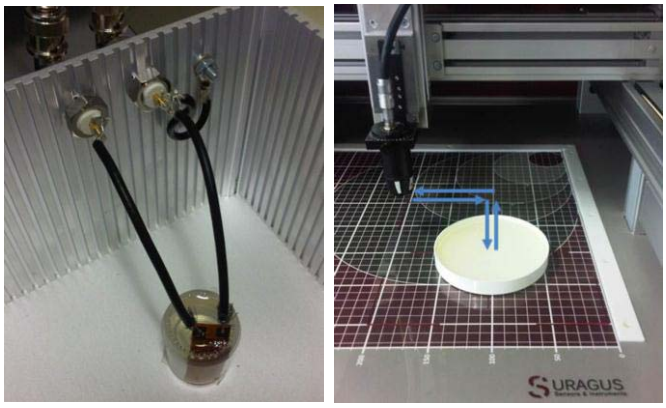

Fig. 7. Experimental setup. Left: capacitive measurement. Right: HFEC measurement.

The capacitive reference setup consisted of an *LCR* meter (HP4275A) connected to a comb electrode (Netzsch IDEX, Model 065S A/D, Ratio 80), built within a Faraday cage. About 20 g of the resin system were filled into a small cup (25-mm diameter and 30-mm high), and placed in the faraday cage immediately after mixing (Fig. 7). The electrode was dipped into this cup until it was completely covered by resin. Capacitance C and dissipation factor D were measured at the frequencies 2 and 4 MHz and manually recorded every 5 min for the first 2 h. Later, the measurement interval was increased.

For the HFEC measurement, the industrial device EddyCUS CF map 4040 from Suragus and a specifically designed permittivity sensor named RD-P020B was used. The probe has an outer diameter of 24 mm, a coil diameter of 2 mm, and the highest sensitivity at 6 MHz. The manipulator of the device was used for a one-point measurement with a controlled, 1-mm liftoff between the sample and the probe. In addition, the mapping device made it possible to overcome the temperature effects caused by the exothermal curing reaction. The sensor was not permanently located at the measurement position, but parked at a reference position between two measurements. When the reference position was reached, a no sample measurement (air) was conducted for calibration purpose. Every 60 s, the sensor moved to the measurement position. There, $\sim$100 g of the epoxy resin was placed in a plastic cup (112-mm diameter and 15-mm high, Fig. 7). Movement and automated recording of the measurement data was realized by a software tool developed at Fraunhofer IKTS MD (former Fraunhofer IZFP, Dresden). HFEC measurements were conducted at 2 and 6 MHz. The LCR meter that was used for the capacitive reference setup was restricted to frequencies of 2, 4, and 10 MHz. Unfortunately, the HFEC sensor showed a low signal-to-noise ratio at 4 and 10 MHz, so 6 MHz was selected as the second measurement frequency.

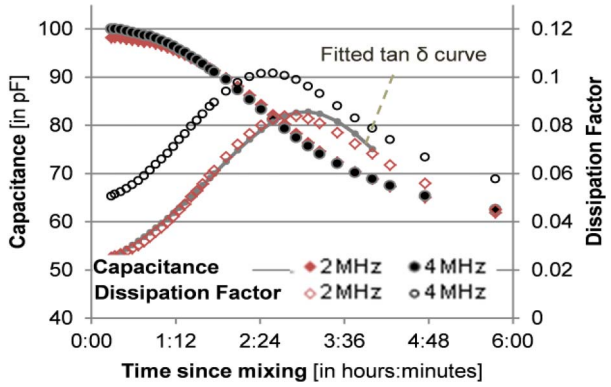

Fig. 8. Capacitive measurement during cure of epoxy resin L20: capacity as a measure for real part of permittivity and dissipation factor proportional to tan δ of permittivity.

For a better comparison of the two different measurement technologies, curves were fitted to the tan δ values obtained at 2 MHz using the Excel solver (minimizing the sum of squares of deviations). Following the approach of [38] and [49], a classical Debye model [50] was used for modeling chemical reactions in solutions. Thus, $\tan\delta$ can be expressed as a function of the reaction time t, the angular frequency ω, and the four fitting parameters, namely, static permittivity ε_s, high-frequency unrelaxed permittivity ε_∞, the material-dependent time constants a, and the material-dependent inverse time constant k

$$\tan\delta = \frac{\varepsilon_s - \varepsilon_\infty}{\varepsilon_\infty + \dfrac{\varepsilon_s - \varepsilon_\infty}{1+\omega^2\tau^2}} * \frac{\omega\tau}{1+\omega^2\tau^2} \tag{13}$$

with $\tau = ae^{kt}$.

Using (13), the time t_m, when the peak in the dissipation factor occurs, can be described

$$t_m = \ln\left(\frac{\varepsilon_s}{a^2\varepsilon_\infty\omega^2}\right)\Big/2k. \tag{14}$$

As the model is designed for chemical reactions in solutions, the fit only works well up to a certain degree of vitrification. We considered this point by only fitting the measurement data of the first 4 h.

C. Results of the Capacitive Reference Measurement

The permittivity change during cure (Fig. 8), which was observed qualitatively via the comb electrode, shows the typical characteristics that we described earlier. For quantification, the permittivity of the substrate material and capacity of the cables must be considered. This could be done by experimental calibration measurements with a well-known fluid or alternatively by model-based expost corrections of the measured values [51]. The model-based approach requires the permittivity value of the substrate material [52], which was not available. Likewise, a well-known liquid reference material, where complex permittivity is exactly listed for 2 and 4 MHz, could not be identified. As both permittivity of the substrate as well as capacity of the cables stay almost constant during cure, they do not influence the qualitative cure monitoring at a constant frequency. Only when comparing different frequencies, it is important to keep those influences in mind.

Focusing at one measurement frequency, it can be seen that the capacitance decreases during cure. It depends on the real part of permittivity [10], [51] and shows the typical characteristics (as summarized in Section IV-A) that we would have expected regarding a permittivity change of an epoxy resin during cure. At first, the decrease is slow (about −0.05 pF/min). About 90 min after mixing (which is also the pot time of this epoxy system), permittivity drops much faster for the next 3–4 h (Fig. 8, about −0.2 pF/min). Then, the capacitance decrease slows down again. When comparing the acquired data from 4 to 2 MHz (Fig. 8), the expected time shift between both capacitance curves (Fig. 6) cannot be seen clearly. Probably, the difference in frequency is too small. Instead, at higher frequencies, a higher capacitance is measured; within the resin as well as without sample. However, this does not necessarily mean that the initial permittivity differs between 2 and 4 MHz. The cables and the electrode, which are not designed for such high frequencies, may influence the signal. This argument is supported by the fact that even in air, the measured capacitance rises with increasing frequency.

Looking at the dissipation factor $\tan(\delta)$ (Fig. 8), a rather good agreement with the expected behavior is observed. It shows a clear maximum during cure, which is reached earlier at higher frequencies. For 2-MHz, fitting parameters were estimated with $\varepsilon_s = 5.72$, $\varepsilon_\infty = 4.82$, $a = 1.06\text{E}{-}08$ s, and $k = 1.91\text{E}{-}04\ \text{s}^{-1}$ at a mean squared error of $0.4\text{E}{-}05$ between the measured and estimated $\tan\delta$. The time when the peak occurs was estimated at $t_m = 10\,978$ s.

D. Results of the HFEC Measurement

Using an HFEC device, it is possible to qualitatively monitor the permittivity change of an epoxy resin during cure. A very good agreement was found between the HFEC data and those obtained with the capacitive reference approach.

The right processing of raw data is crucial for an accurate interpretation of the results obtained by HFEC devices (Fig. 10). For each EC measurement value, a corresponding reference value in air was taken by moving the sensor away from the sample, using the gantry of the scanner. These air values are used to reference each measurement value to air, and hence to eliminate temperature and long-term drift effects. Consequently, only the impedance difference Z between air and the sample is evaluated. Thus, the measured permittivity needs to be interpreted as a permittivity difference to air. This approach is widely used in EC measurement [1]. However, it is assuming an additive influence of drift.

In addition to the drift effects, it is also important to correct the frequency-dependent phase offset caused by the measurement system itself [53]. The phase of the measured impedance values is important for determining its real and imaginary parts, as well as the right $\tan\delta$. A numerical solution for correcting the phase offset has not yet been found. Hence, we made use of the capacitive reference values.

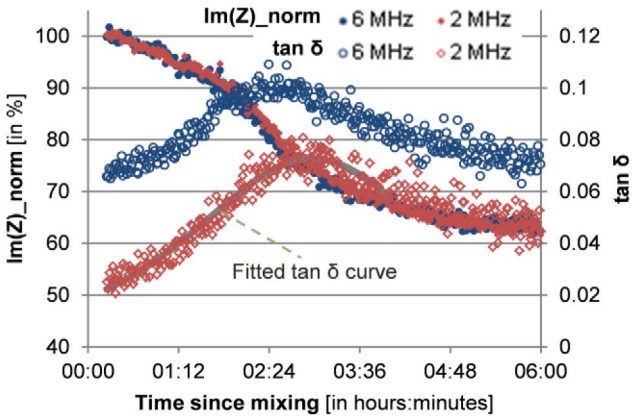

Fig. 9. Measurement with HFEC device during cure of epoxy resin L20: normalized imaginary part of complex impedance as a measure for real part of permittivity and tan δ of impedance analog to tan δ of permittivity.

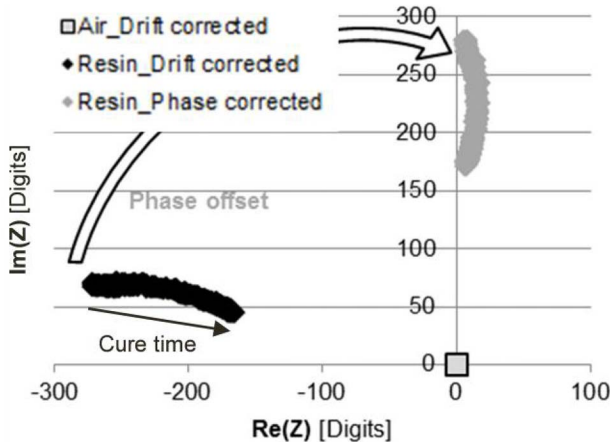

Fig. 10. Principle of phase offset correction and final set of data (gray).

The phase offset was defined as follows. The tan δ of the first EC measurement was set to be equal to the dissipation factor measured with the capacitive approach at 2 MHz and to meet the dissipation factor calculated for 6 MHz by applying a Debye model [50] to the 2-MHz value. This might be inappropriate for a quantitative measurement (as the capacitive values are not exact either and tan δ of air is neglected), but for a qualitative comparison it should be sufficient.

The data set derived after processing the raw values can be used for analyzing the change of the complex impedance over cure time (Fig. 9). From Maxwell's equations (1)–(4) and the FEM simulation (Sections II and III), we know that the change of the imaginary part of impedance represents the change of the real part of permittivity, whereas the real part of impedance is influenced by a changing dielectric loss. Subsequently, when comparing the HFEC measurement results to the capacitance and dissipation factor data obtained by the capacitive reference measurement, the change of the imaginary part of the complex impedance Z and the ratio real to imaginary part of complex impedance (tan δ) should be used. To enhance comparability of two measurement frequencies, we additionally normalized the imaginary part of the complex impedance Z (using the average of the first five measurements).

Now, comparing the results obtained with the HFEC device to those measured with the capacitive reference setup, a high similarity can be seen. All the typical characteristics of the capacitive reference measurement are present in the HFEC data as well—such as the typical progression of relative permittivity or the frequency-dependent peak in dissipation losses tan δ. Even the relative change of permittivity is very consistent. At 2 MHz, the tan δ curve fitting parameters were estimated with $\varepsilon_s = 5.59$, $\varepsilon_\infty = 4.83$, $a = 1.13\text{E}{-}08$ s, and $k = 1.90\text{E}{-}04$ s^{-1} at a mean squared error of $1.73\text{E}{-}05$ between the measured and estimated tan δ. The time when the peak occurs was estimated with $t_m = 10\,680$ s. This is $\sim$5 min earlier than the estimated peak of the capacitive setup. This deviation is $<3\%$, which is quite small regarding possible experimental differences in mixing ratio and room temperature as well as fitting uncertainties. The most significant difference is the higher scattering of the values measured with the HFEC device, resulting in a higher mean squared error for the fitting function. One explanation might be a slight deviation of the sensor position for each measurement. The probe can repetitively return to a position with an accuracy <100 μm. Compared with the 1-mm liftoff, this is still a significant deviation. Improving mechanics for the sensor movement, using an advanced sensor design and measuring at higher frequencies should reduce the scatter drastically. In addition, enhanced data processing, such as averaging of raw data or curve fitting, might be another possibility to improve the quality of HFEC cure monitoring.

However, the example of cure monitoring was selected to qualitatively prove the concept of permittivity measurement using HFEC devices in a favorable setup for this technology (see the introduction in Section IV). For an industrial application, in this field, HFEC will need to demonstrate its advantages compared with the capacitive measurement [49], [51] and microwave cure monitoring [54], [55]. At the moment, HFEC devices are not achieving measurement accuracies that are comparable with contacting capacitive or microwave methods. Nevertheless, for applications where this accuracy is not critical, HFEC measurement could be a robust and simple alternative [56] for qualitative cure monitoring. A calibration (using a known sample or a capacitive reference setup) is needed to determine the phase offset for a specific measurement frequency of a specific sensor. That calibration either could be done at the manufacturer of the HFEC device for each system, which is sold for permittivity measurement, or directly at the customer. If it should be done at the customer calibration samples with a known complex permittivity and a good instruction or even software for calibration should be supplied with the sensor. That would make especially sense for customers, who already own an HFEC device and want to use it additionally for permittivity characterization. Once calibrated, the system can be used for different resins and does not require contact to the sample.

V. Permittivity Imaging

In addition to the single-point permittivity measurement described in the previous section, a qualitative permittivity image can be acquired by moving an HFEC probe over

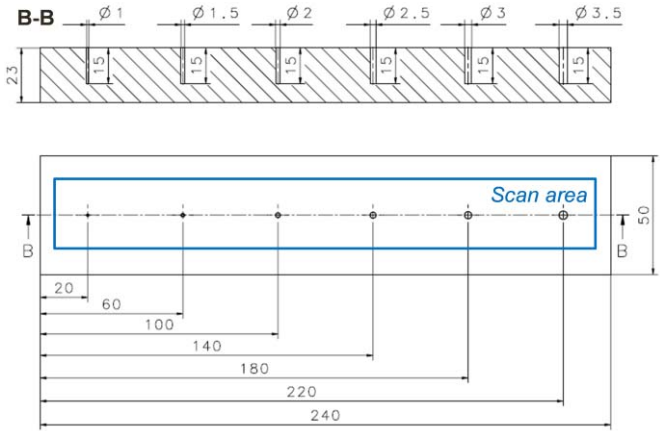

Fig. 11. Specification of sample 1, measures in millimeter.

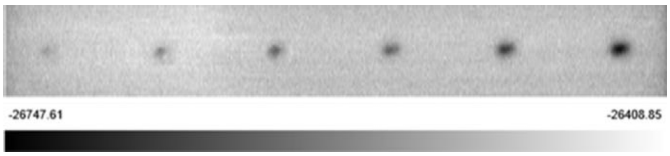

Fig. 12. HFEC image of sample 1, measurement values in digits.

a dielectric material. A potential application would be the homogeneity control of the permittivity after the resin is cured. This is a good indicator for the degree of cross linking [10] or the detection of defects below the surface.

In addition to the proof-of-concept for HFEC permittivity mapping on insulating materials, this section should serve as a first experimental comparison with capacitive imaging. Therefore, we produced our samples according to the specifications mentioned in [12].

Sample 1 is a 240 mm × 50 mm × 25-mm polymethyl methacrylate (PMMA) plate, which contains six 15-mm deep holes of different diameters (Fig. 11). It was characterized using the industrial device EddyCUS CF map 4040 from Suragus combined with the sensor RD-P007B. This probe was particularly designed for permittivity mapping. It has an outer diameter of 16 mm, a coil diameter of 0.7 mm (allowing a high spatial resolution), and is especially sensitive at 1.75 and 3.5 MHz. An area of 30 mm × 230 mm was scanned at 3.5 MHz and 25 dB, using a pitch of 0.2 mm × 1 mm. To avoid liftoff variations, the sample was scanned in contact with the sensor.

The resulting HFEC image (Fig. 12) shows all holes, even the smallest one with only 1-mm diameter. Compared with the results reported in [12], the HFEC image shows a significantly better spatial resolution and a comparable or even slightly better sensitivity.

Sample 2 is a 240 mm × 90 mm × 10-mm PMMA plate containing four 20 mm × 20-mm flat-bottomed holes of different depths—2, 4, 6, and 8 mm (Fig. 13). As opposed to the first sample, this time the sensor RD-P020B was used, which was already introduced in Section IV. An area of 195 mm × 45 mm was scanned at 6 MHz, 32 dB, using a pitch of 0.2 mm × 1 mm, once from faces A and B.

The resulting HFEC image from face A (Fig. 14 contains information on the depth of the holes (grayscale).

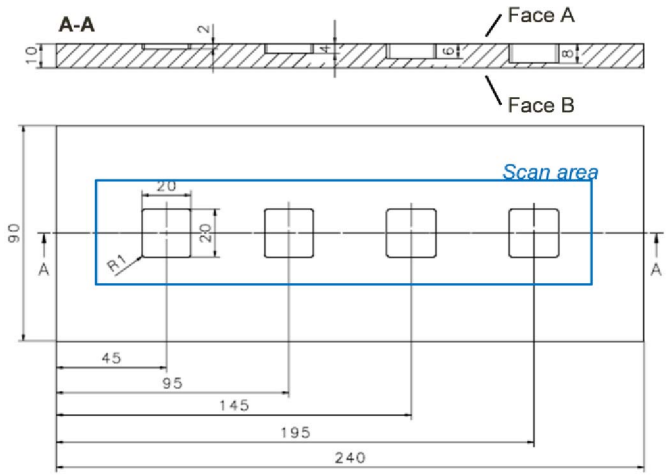

Fig. 13. Specification of sample 2, measures in millimeter.

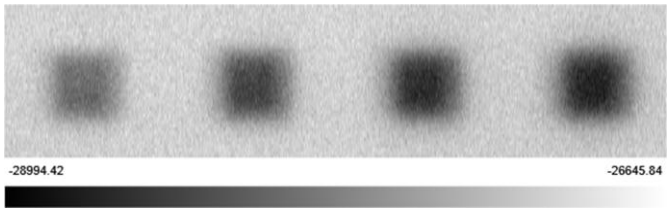

Fig. 14. HFEC image of sample 2, face A. Measurement values in digits.

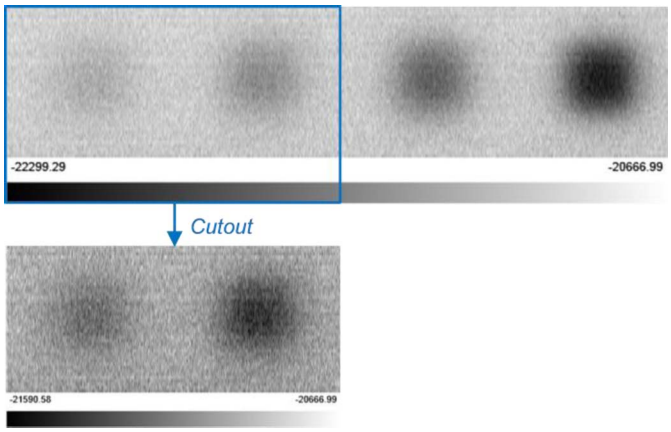

Fig. 15. HFEC image of sample 2, face B and cutout with adjusted gray scale. Measurement values in digits.

This is another advantage compared with the capacitive imaging results reported in [12]. Again, the better spatial resolution of HFEC measurement is evident.

The HFEC image from face B (Fig. 15) proofs that the technology is able to detect hidden defects in insulating materials like PMMA. All holes, up to 8 mm below the sample surface, have been detected. The depth of the defect is visible in its gray shade, but mixed with the information on defect size (depth). However, with increasing distance to the surface, it becomes more difficult to see the exact shape of the defect. In comparison with the capacitive imaging results reported in [12], it can be seen that HFEC shows a better visibility of the holes near the sample surface, whereas capacitive imaging achieves a better contrast for defects further away from the sample surface.

In general, capacitive imaging has the advantage that it is not influenced by magnetic properties of the sample. In addition, the detection of planar cracks, parallel to the sample surface might be easier due to the direction of the electric field [3], [4]. However, an HFEC device might be more suitable to detect planar cracks, which are orthogonal to the sample surface or for measurement tasks where the sample surface is covered by a thin conductive layer. In addition, the HFEC device can be used for various other applications on conductive materials as well, which might be especially advantageous for small laboratories.

VI. Conclusion

Our research demonstrates that HFEC devices, operating in the megahertz frequency range, can not only be used for characterization of electrically conductive materials, but also for imaging and investigation of insulating samples. In this case, it is the complex permittivity of the material, which is influencing the complex impedance. The experimental evidence was given by monitoring the permittivity change during cure and by mapping defects in insulators. Potential advantages of HFEC permittivity measurements compared with capacitive imaging were identified (higher spatial resolution and defect depth indication). However, all the presented results were qualitatively and only attained on insulating samples. Maxwell's equations and FEM simulations give the indication that sample permittivity also influences the HFEC measurement of low conductive samples. In addition, there is the hypothesis that the sample permittivity is part of the HFEC response even when characterizing CFRP [23], [30].

A focus of future research, therefore, needs to address the following two topics.

1) The evaluation of measurement accuracy regarding quantitative permittivity characterization using a calibration curve. It is important to know the potential of HFEC to evaluate the tradeoff between the saving of sample preparation but lower measurement accuracy.
2) To evaluate the potential of HFEC for permittivity characterization of low conductive, highly anisotropic materials like multidirectional CFRP. On insulation materials, the technology is able to compete with capacitive imaging but not to compete against spatial resolution of microwave or terahertz systems (e.g., evanescent microwave probe imaging has a 0.4-μm lateral spatial resolution at 1 GHz [4]). Multidirectional CFRP is the application where most existing permittivity characterization methods fail. Contacting capacitive methods suffer from electrode polarization [7], [10], capacitive imaging only allows surface characterization due to accumulating charges on the sample surface [12] and high-frequency methods, which are operating in the microwave or terahertz frequency range, only allow penetration into unidirectional CFRPs [5], [15]. When evaluating the use of HFEC for permittivity measurement in CFRP, a major part of the work is not only evaluation of the possibility of permittivity characterization but also the separation of the different sample properties that are influencing the HFEC signal.

References

[1] *Non-Destructive Testing—Eddy Current Testing—General Principles*, ISO Standard 15549, 2008.

[2] A. Yashan, "Über die Wirbelstromprüfung und magnetische Streuflussprüfung mittels GMR-Sensoren," Ph.D. dissertation, Dept. Mater. Sci., Univ. Saarlandes, Saarbrücken, Germany, 2008.

[3] G. G. Diamond and D. A. Hutchins, "A new capacitive imaging technique for NDT," presented at the Eur. Conf. NDT, Berlin, Germany, Sep. 2006.

[4] M. Tabib-Azar, P. S. Pathak, G. Ponchak, and S. LeClair, "Nondestructive superresolution imaging of defects and nonuniformities in metals, semiconductors, dielectrics, composites, and plants using evanescent microwaves," *Rev. Sci. Instrum.*, vol. 70, no. 6, pp. 2783–2792, Jun. 1999.

[5] S. Kharkovsky and R. Zoughi, "Microwave and millimeter wave nondestructive testing and evaluation—Overview and recent advances," *IEEE Instrum. Meas. Mag.*, vol. 10, no. 2, pp. 26–38, Apr. 2007.

[6] *Nomenclature of the Frequency and Wavelength Bands Used in Telecommunications*, document Rec. ITU-R V.431–7, 2000.

[7] J. Mijović, J. Kenny, A. Maffezzoli, A. Trivisano, F. Bellucci, and L. Nicolais, "The principles of dielectric measurements for *in situ* monitoring of composite processing," *Compos. Sci. Technol.*, vol. 49, no. 3, pp. 277–290, 1993.

[8] A. A. Nassr and W. W. El-Dakhakhni, "Non-destructive evaluation of laminated composite plates using dielectrometry sensors," *Smart Mater. Struct.*, vol. 18, no. 5, p. 055014, 2009.

[9] *Alpha-A High Resolution Dielectric, Conductivity, Impedance and Gain Phase Modular Measurement System*, Novocontrol Technologies, Montabaur, Germany, 2004.

[10] A. R. Blythe and D. Bloor, *Electrical Properties of Polymers*, 2nd ed. New York, NY, USA: Cambridge Univ. Press, 2005, pp. 27–185.

[11] R. A. Pethrick, "Non-destructive evaluation of composites: Dielectric techniques for testing partially or non-conducting composite materials," in *Non-Destructive Evaluation (NDE) of Polymer Matrix Composites: Techniques and Applications*, V. M. Karbhari, Ed. Cambridge, U.K.: Woodhead Pub., 2013, pp. 116–135.

[12] X. Yin, D. A. Hutchins, G. Chen, and W. Li, "Investigations into the measurement sensitivity distribution of coplanar capacitive imaging probes," *NDT & E Int.*, vol. 58, pp. 1–9, Sep. 2013.

[13] A. W. Kraszewski, "Microwave aquametry—A review," *J. Microw. Power*, vol. 15, no. 4, pp. 209–220, 1980.

[14] M. S. Venkatesh and G. S. V. Raghavan, "An overview of dielectric properties measuring techniques," *Can. Biosyst. Eng.*, vol. 47, no. 7, pp. 15–30, 2005.

[15] L. Diener, "Microwave near-field imaging with open-ended waveguide—Comparison with other techniques of nondestructive testing," *Res. Nondestruct. Eval.*, vol. 7, nos. 2–3, pp. 137–152, 1995.

[16] R. Zoughi, *Microwave Non-Destructive Testing and Evaluation Principles*. Dordrecht, The Netherlands: Kluwer, 2000.

[17] R. Zoughi and S. Kharkovsky, "Microwave and millimetre wave sensors for crack detection," *Fatigue Fract. Eng. Mater. Struct.*, vol. 31, no. 8, pp. 695–713, 2008.

[18] J. H. Hinken, "Mikrowellenbasierte zerstörungsfreie Prüfung," *ZfP-Zeitung*, vol. 104, pp. 37–42, Apr. 2007.

[19] T. Beller, J. H. Hinken, and M. Voigt, "Hochauflösende Mikrowellen-Defektoskopie," in *Proc. DGzfP Zerstörungsfreie Materialprüfung*, Fürth, Germany, 2007, p. V53.

[20] M. Pastorino, "Recent inversion procedures for microwave imaging in biomedical, subsurface detection and nondestructive evaluation applications," *Measurement*, vol. 36, nos. 3–4, pp. 257–269, 2004.

[21] M. Abu-Khousa, W. Saleh, and N. Qaddoumi, "Defect imaging and characterization in composite structures using near-field microwave nondestructive testing techniques," *Compos. Struct.*, vol. 62, nos. 3–4, pp. 255–259, 2003.

[22] A. Redo-Sanchez, N. Karpowicz, J. Xu, and X. C. Zhang, "Damage and defect inspection with terahertz waves," in *Proc. 4th Int. Workshop Ultrason. Adv. Methods Nondestruct. Test. Mater. Characterization*, 2006, pp. 67–78.

[23] M. H. Schulze, H. Heuer, M. Küttner, and N. Meyendorf, "High-resolution eddy current sensor system for quality assessment of carbon fiber materials," *Microsyst. Technol.*, vol. 16, no. 5, pp. 791–797, 2010.

[24] H. Heuer, M. H. Schulze, and N. Meyendorf, "Non-destructive evaluation (NDE) of composites: Eddy current techniques," in *Non-Destructive Evaluation (NDE) of Polymer Matrix Composites: Techniques and Applications*, V. M. Karbhari, Ed. Cambridge, U.K.: Woodhead Pub., 2013, pp. 33–55.

[25] D. J. Hagemaier, "Eddy-current standard depth of penetration," *Mater. Eval.*, vol. 43, no. 11, pp. 1438–1441, 1985.
[26] Z. Mottl, "The quantitative relations between true and standard depth of penetration for air-cored probe coils in eddy current testing," *NDT Int.*, vol. 23, no. 1, pp. 11–18, 1990.
[27] M. P. De Goeje and K. E. D. Wapenaar, "Non-destructive inspection of carbon fibre-reinforced plastics using eddy current methods," *Composites*, vol. 23, no. 3, pp. 147–157, 1992.
[28] C. Beine *et al.*, "NDT for CFRP aeronautical components—A comparative study," presented at the 2nd Int. Symp. NDT Aerosp., Hamburg, Germany, Nov. 2010.
[29] C. Hellier, *Handbook of Nondestructive Evaluation*. New York, NY, USA: McGraw-Hill, 2003.
[30] R. Lange and G. Mook, "Structural analysis of CFRP using eddy current methods," *NDT & E Int.*, vol. 27, no. 5, pp. 241–248, 1994.
[31] S. K. Brady, "Exploiting changes in dielectric dissipation to detect thermal degradation in polymers and composites," *Rev. Progr. Quant. Nondestruct. Eval.*, vol. 29, no. 1, pp. 1087–1094, 2010.
[32] J. C. Maxwell, "A dynamical theory of the electromagnetic field," *Philosoph. Trans. Roy. Soc. London*, vol. 155, pp. 459–512, Jan. 1865.
[33] J. García-Martín, J. Gómez-Gil, and E. Vázquez-Sánchez, "Non-destructive techniques based on eddy current testing," *Sensors*, vol. 11, no. 12, pp. 2525–2565, 2011.
[34] ANSYS. (Mar. 2012). *Maxwell 3D User's Guide: Software Version 15*. [Online]. Available: http://www.mae.ncsu.edu/buckner/courses/mae535/Maxwell3D.pdf
[35] J. Hansen, "The eddy current inspection method. Part 2: The impedance plane and probes," *Insight*, vol. 46, no. 6, pp. 364–365, 2004.
[36] H. Block, "The nature and application of electrical phenomena in polymers," in *Electric Phenomena in Polymer Science* (Advances in Polymer Science), vol. 33, H.-J. Cantow, Ed. Berlin, Germany: Springer-Verlag, 1979, pp. 93–167.
[37] G. W. Ehrenstein, E. Bittmann, and L. Hoffmann, *Duroplaste: Aushärtung—Prüfung—Eigenschaften*. München, Germany: Hanser, 1997, pp. 1–19 and 69–75.
[38] S. Wu, S. Gedeon, and R. A. Fouracre, "The measurement and modeling of the dielectric response of molecules during curing of epoxy resin," *IEEE Trans. Electr. Insul.*, vol. 23, no. 3, pp. 409–417, Jun. 1988.
[39] J. Mijović and B. D. Fitz. (1998). *Dielectric Spectoskopy of Reactive Polymers. Novocontrol Application Note Dielectrics 2*. [Online]. Available: http://www.novocontrol.de/pdf_s/APND2.PDF
[40] A. Schönhals, "6.3 Elektrische und dielektrische Eigenschaften," in *Kunststoffprüfung*, W. Grellmann and S. Seidler, Eds. München, Germany: Carl Hanser Verlag, 2005, pp. 352–404.
[41] N. F. Sheppard and S. D. Senturia, "Chemical interpretation of the relaxed permittivity during epoxy resin cure," *Polym. Eng. Sci*, vol. 26, no. 5, pp. 354–357, 1986.
[42] D. Kranbuehl *et al.*, "Use of the frequency dependence of the impedance to monitor viscosity during cure," *Polym. Eng. Sci.*, vol. 29, no. 5, pp. 285–289, 1989.
[43] Y. A. Tajima, "Monitoring cure viscosity of epoxy composite," *Polym. Compos.*, vol. 3, no. 3, pp. 162–169, 1982.
[44] A. Shiota and C. K. Ober, "Orientation of liquid crystalline epoxides under ac electric fields," *Macromolecules*, vol. 30, no. 15, pp. 4278–4287, 1997.
[45] B. C. Benicewicz *et al.*, "Magnetic field orientation of liquid crystalline epoxy thermosets," *Macromolecules*, vol. 31, no. 15, pp. 4730–4738, 1998.
[46] M.-K. Schwarz, W. Bauhofer, and K. Schulte, "Alternating electric field induced agglomeration of carbon black filled resins," *Polymer*, vol. 43, no. 10, pp. 3079–3082, 2002.
[47] C. A. Martin *et al.*, "Electric field-induced aligned multi-wall carbon nanotube networks in epoxy composites," *Polymer*, vol. 46, no. 3, pp. 877–886, 2005.
[48] J. Mijovic and J. Wijaya, "Comparative calorimetric study of epoxy cure by microwave vs thermal energy," *Macromolecules*, vol. 23, no. 15, pp. 3671–3674, 1990.
[49] J. Delmonte, "Electrical properties of epoxy resins during polymerization," *J. Appl. Polym. Sci.*, vol. 2, no. 4, pp. 108–113, 1959.
[50] P. Debye, *Polare Molekeln*. Leipzig, Germany: Hirzel, 1929.
[51] S. D. Senturia and N. F. Sheppard, "Dielectric analysis of thermoset cure," in *Advances in Polymer Science*. Berlin, Germany: Springer-Verlag, 1986, pp. 1–47.
[52] F. Starzyk, "Parametrisation of interdigit comb capacitor for dielectric impedance spectroscopy," *Archives Mater. Sci. Eng.*, vol. 34, no. 1, pp. 31–34, 2008.
[53] D. Joneit, M. Nadler, and H. Heuer, "Correction of eddy current measurements to obtain accordance with simulation results," *NDT & E Int.*, vol. 62, pp. 167–171, Mar. 2014.
[54] S. Carrozzino, G. Levita, P. Rolla, and E. Tombari, "Calorimetric and microwave dielectric monitoring of epoxy resin cure," *Polym. Eng. Sci.*, vol. 30, no. 6, pp. 366–373, 1990.
[55] C. Carlini, P. A. Rolla, and E. Tombari, "Measurement method and apparatus for monitoring the kinetics of polymerization and crosslinking reactions by microwave dielectrometry," *J. Appl. Polym. Sci.*, vol. 41, nos. 3–4, pp. 805–818, 1990.
[56] X. E. Gros, K. Ogi, and K. Tagahashi, "Eddy current, ultrasonic C-scan and scanning acoustic microscopy testing of delaminated quasi-isotropic CFRP materials: A case study," *J. Reinforced Plastics Compos.*, vol. 19, no. 5, pp. 389–405, 1998.

Simone Gäbler received the Diploma degree in business and engineering from the Dresden University of Technology (TU Dresden), Dresden, Germany, in 2010, where she is currently pursuing the Ph.D. degree in mechanical engineering.

She is currently a Research Assistant with the Leibniz Institute of Polymer Research, Dresden, and a Visiting Researcher with the Fraunhofer Institute for Ceramic Technologies and Systems-Materials Diagnostics, Dresden. Her current research interests include the development of eddy current testing technology for the characterization of polymers and composites.

Ms. Gäbler received a scholarship from TU Dresden. She was a recipient of the Viktor-Klemperer Certificate of TU Dresden and the Award of the Faculty of Business and Economics, both for outstanding performance during her studies, and the DPG Award for exceptional A-levels in Physics.

Henning Heuer received the Diploma degree from the Dresden University of Technology (TU Dresden), Dresden, Germany, and the Ph.D. degree in electrical engineering and microelectronics from Brandenburg University of Technology (TU Cottbus), Cottbus, Germany, in 2005.

He became a Junior Professor and the Chair of the Sensor Systems for Nondestructive Testing at TU Dresden, in 2012. He is also the Head of the Department of Sensors and Sensor Systems with the Fraunhofer Institute for Ceramic Technologies and Systems-Materials Diagnostics (IKTS-MD), Dresden. The department focuses on the development of inspection techniques for new generations of materials and technical structures. With his strong background in semiconductors and their packaging and assembly technologies, his team developed ultrasonic phased array sensor for special applications. Also, new solutions for eddy current based inspection systems, the high frequency platform EddyCus were developed. The company SURAGUS GmbH is a spin off from his team at Fraunhofer IKTS-MD in Dresden. His current research interests include the eddy current and ultrasonic sensors and sensor systems.

Gert Heinrich received the Diploma degree in theoretical physics from Friedrich-Schiller University Jena, Jena, Germany, in 1973, and the Ph.D. degree in polymer physics and the Habilitation degree from the University of Technology at Merseburg, Merseburg, Germany, in 1977 and 1986, respectively.

He taught theoretical physics, polymer physics, and rubber physics as an Assistant Professor and as an Associate Professor with the University of Technology at Merseburg, from 1978 to 1990. He was a Senior Research Scientist and the Head of the Materials Research with the Research and Development, Strategic Technology Centre, Continental AG, Hannover, Germany, from 1990 to 2002. He has been a Professor of Polymer Materials Science and Rubber Technology with the Institute of Materials Science, Dresden University of Technology, Dresden, Germany, and the Director of the Institute of Polymer Materials with the Leibniz Institute of Polymer Research Dresden, Dresden, since 2003. He has contributed to various aspects of the science, technology and education of polymer materials and rubbers, in particular, statistical theory of polymer networks, rubber friction and tire materials physics, predictive testing, reinforcement and its molecular and mathematical basis, and polymer nanocomposites.